ADVANCED FUNCTIONAL MATERIALS
www.afm-journal.de

Oxygen Ion Pumping across Atomically Designed Oxide Heterointerfaces

*Yongshun Wu, Yang Zhang, Jianbing Zhang, Yingjie Lyu, Cong Li, Sijie Wu, Yupu Wang, Meng Wang, Youwen Long, Tianxiang Nan, Di Yi, Junyi Zhu, Qing He, Shuyun Zhou, and Pu Yu**

Complex oxide heterointerfaces and heterostructures have demonstrated enormous emergent phenomena over the last decades, attributed to the reconstructions of mis-matched crystalline structure, polarity, and spin ordering across the heterointerfaces. This work employs the heterostructures of $La_{0.7}Sr_{0.3}MnO_3$ and $CaFeO_{2.5}$ as model system to demonstrate an interface-specific oxygen migration/reconstruction across the interfaces due to the mismatched chemical potential, which dramatically influences the ferromagnetic and electronic states of $La_{0.7}Sr_{0.3}MnO_3$ layer. Specifically, the alternative stacking of octahedral (O_h) and tetrahedral (T_d) layers in $CaFeO_{2.5}$ are used to form two distinct heterointerfaces, namely the O_h-T_d and the O_h-O_h interfaces with the adjacent $La_{0.7}Sr_{0.3}MnO_3$ layer. Interestingly, the oxygen ion migrates toward opposite directions across the interface for these two cases, in which the $CaFeO_{2.5}$ layer acts as an "oxygen pump" and manipulates the oxygen contents of its adjacent $La_{0.7}Sr_{0.3}MnO_3$ layers. Such manipulation leads to a dramatically changed ferromagnetic transition temperature for the heterostructure with the O_h-T_d and O_h-O_h interface. This work establishes a feasible and efficient strategy to control the oxygen ionic distribution through atomic-scale interface design and opens up new opportunities to exploit emergent states at the complex oxide heterostructures through selective oxygen ion evolution.

1. Introduction

Over the past few decades, complex oxide heterostructures/heterointerfaces have been developed as an exciting platform to design and explore emergent phenomena and advanced functionalities absent in corresponding bulk materials.[1–4] This excellent opportunity is primarily offered by the mismatched lattice, charge, and spin degrees of freedom across the heterointerfaces. For instance, the mismatched lattice constant leads to epitaxial strain and enforces the lattice deformation into the functional layer to manipulate its magnetic and electronic states[5–7]; while the discontinuity of the spin ordering at the interface can lead to spin frustrations with emergent magnetism.[8,9] Besides these, the mismatched charge degree of freedom (electrostatic potential) is particularly fascinating because it can result in charge transfer across the interface, leading to substantial modification of the electronic states in

Y. Wu, Y. Zhang, J. Zhang, Y. Lyu, C. Li, S. Wu, Y. Wang, S. Zhou, P. Yu
State Key Laboratory of Low Dimensional Quantum Physics and Department of Physics
Tsinghua University
Beijing 100084, China
E-mail: yupu@mail.tsinghua.edu.cn

Y. Wang, J. Zhu
Department of Physics
Chinese University of Hong Kong
Hong Kong SAR 999077, China

M. Wang
School of Integrated Circuits and Electronics
MIIT Key Laboratory for Low-Dimensional Quantum Structure and Devices
Beijing Institute of Technology
Beijing 100081, China

Y. Long
Beijing National Laboratory for Condensed Matter Physics
Institute of Physics
Chinese Academy of Sciences
Beijing 100190, China

T. Nan
School of Integrated Circuits
Beijing National Research Center for Information Science and Technology
Tsinghua University
Beijing 100084, China

D. Yi
State Key Laboratory of New Ceramics and Fine Processing
School of Materials Science and Engineering
Tsinghua University
Beijing 100084, China

Q. He
Department of Physics
Durham University
Durham DH13LE, UK

S. Zhou, P. Yu
Frontier Science Center for Quantum Information
Beijing 100084, China

The ORCID identification number(s) for the author(s) of this article can be found under https://doi.org/10.1002/adfm.202407046

DOI: 10.1002/adfm.202407046

the heterostructures.[2,10–13] For instance, attaching a polar material (e.g., $LaAlO_3$, LAO) to a non-polar material (e.g., $SrTiO_3$, STO) can result in distinct charge reconstructions depending on the atomic stacking sequence at the interface. Specifically, when a few unit cells of LAO are grown on TiO_2 terminated STO, 2D electron gas (2DEG) is formed at the interface,[2] which was first attributed to the electron transfer from the LAO surface to the interface based on the so-called polar catastrophe mechanism.[10] However, it is nowadays widely recognized that oxygen ion also plays a critical role in the formation of 2DEG.[14–16]

Manipulating oxygen vacancy, the most common defect in complex oxides, is a straightforward pathway to tailor the properties of oxides, such as magnetism,[17,18] superconductivity,[19] metal-to-insulator transition,[20] ionic conductivity,[21] and even ferroelectricity.[22] Such efficient manipulation arises from two primary factors. First, the creation/annihilation of an oxygen vacancy donates two electrons/holes into the system,[23,24] thereby contributing substantially to the carrier filling. Second, the long-range ordered oxygen vacancies can dramatically change the crystalline symmetry, such as transforming perovskite into grenier,[25] brownmillerites[26–28] and even planar infinite layered structures.[29–31] Because of its charged nature, oxygen vacancy is always coupled with the charge reconstruction across the interface driven by the gradient of electrostatic potential. Additionally, oxygen vacancy can also migrate through the crystal due to the gradient chemical potential of oxygen ions, which is intuitively correlated to the bonding energy of oxygen ions with the transition metal ions.[32] Although artificial control of the oxygen ionic migration is challenging, previous studies have already demonstrated that the chemical potential mismatch between adjacent compounds can lead to oxygen ionic migration across the heterointerfaces.[33–37] Inspired by the concept of polar-catastrophe-governed 2DEG, one might come up with the question that whether this oxygen vacancy migration can be controlled by the atomic stacking at the heterointerfaces. In this work, we employ the heterostructures of the perovskite $La_{0.7}Sr_{0.3}MnO_3$ (LSMO) and brownmillerite (BM) $CaFeO_{2.5}$ (CFO) as a model system to demonstrate an elegant way of controlling the oxygen ionic migration at the heterointerface by delicately design the polyhedral stackings at the heterointerface, which effectively manipulate the magnetic and electronic states of the adjacent LSMO layers.

In this model system, the control of oxygen ion migration direction across the heterointerface is achieved by agilely manipulating the oxygen chemical potential gradient between the adjacent layers. The brownmillerite structure, with alternately stacked by octahedral (O_h) and tetrahedral (T_d) layers, inherently presents a great candidate due to the associated distinct coordination environments. In this study, brownmillerite $CaFeO_{2.5}$ (CFO) was chosen as part of the model system, in which the Fe ions have the coordination numbers of both 6 and 4, corresponding to the octahedral (FeO_6) and tetrahedral (FeO_4) layers, respectively. Despite the distinct local chemical environments, previous studies revealed that the Fe ions hold the robust and identical valence state of Fe^{3+}, [38] which indicates a substantial electron transfer (around one electron per Fe) from the tetrahedral to octahedral layers, predominately via the apical oxygen ions. This fact naturally leads to different chemical potentials for oxygen ions in these layers (T_d and O_h), which nicely fits our design philosophy. Indeed, previous calculations also confirmed that the oxygen vacancy formation energy of equatorial oxygen in FeO_4 T_d is notably lower than that in FeO_6 O_h.[39] To effectively prove the proposed concept, we choose perovskite $La_{0.7}Sr_{0.3}MnO_3$ (LSMO) as the second element of the heterostructure system, as its magnetic and electronic properties are very sensitive to oxygen content.

2. Results and Discussion

We successfully achieve the dual-directional oxygen migration in the perovskite-brownmillerite heterointerfaces by designing two different interfaces, namely T_d-O_h and O_h-O_h with the brownmillerite layer terminated as T_d and O_h, respectively (**Figure 1a**). The key to obtaining these two interfaces relies on the excellent layer-by-layer growth mode of both CFO and LSMO layers. Figure 1b shows typical reflection high-energy electron diffraction (RHEED) intensity oscillations, when CFO is grown on TiO_2-terminated $SrTiO_3$ (STO) (001) substrates (see Experimental Section). Initially, the RHEED intensity oscillation exhibits the characteristics of staggered growth of O_h and T_d layers, and quickly the growth mode turns into the growth of O_h and T_d as a whole block, indicated by the evolution of RHEED intensity into doubled periodicity. These results suggest that the growth of CFO is terminated by the T_d layer due to its relatively lower oxygen vacancy formation energy and the reduced growth environment. Meanwhile, the well-defined RHEED intensity oscillations of LSMO suggest a conventional layer-by-layer growth mode (Figure 1c). Based on these results, the growth sequence of these two layers forms a convenient strategy to control the polyhedral connections (Figure 1d,e and Figure S1, Supporting Information). Specifically, the STO//CFO/LSMO and STO//LSMO/CFO samples grown by RHEED-assisted pulsed laser deposition (Experimental Section) correspond to the T_d-O_h and the O_h-O_h heterointerfaces, respectively.

High-resolution scanning transmission electron microscopy (STEM) measurements were carried out to verify the atomic structures across these heterointerfaces. The high-angle annular dark-field (HAADF-STEM) images in **Figure 2a,b** demonstrate that both heterointerfaces are of high crystalline quality and atomically sharp. Combined with the electron energy loss spectroscopy (EELS) measurements (Figure S2, Supporting Information), the connection across the interfaces between LSMO and CFO can be determined as MnO_2-CaO in both cases (right panel of Figure 2a,b). Annular bright-field (ABF-STEM) images, suitable for imaging light atoms, were obtained to reveal the interfacial polyhedral structures. As depicted in Figure 2c,d, the T_d and O_h layers can be easily identified by the contrast of oxygen atoms. Accordingly, the stacking sequence across the interface is determined as (La, Sr)O-MnO_2-CaO-FeO_2 and FeO-CaO-MnO_2-(La, Sr)O in STO//LSMO/CFO and STO//CFO/LSMO heterostructures, respectively. Thus, both O_h-O_h and T_d-O_h heterointerfaces are achieved as we designed, as the Figure S3, Supporting Information illustrated.

To probe the direction of oxygen ionic migration across these O_h-O_h and T_d-O_h heterointerfaces, we employed the EELS measurements to determine the valence state of Mn ions near the heterointerfaces. Figure 2e,f summarizes the EELS signals of the Mn $L_{3,2}$-edges extracted from five consecutive unit cells (u.c.) of LSMO layers near the interface, where a noticeable "blue shift"

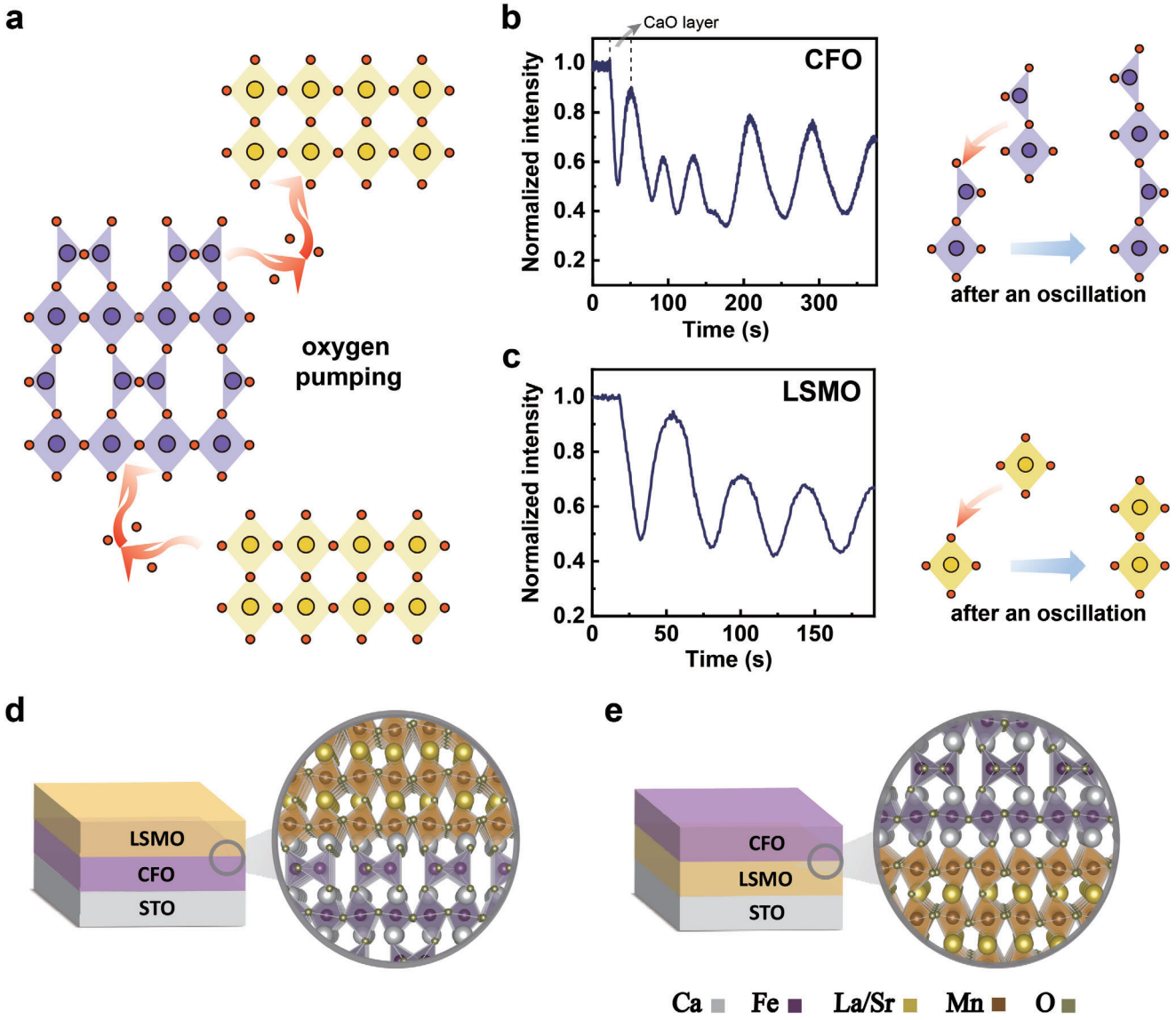

Figure 1. Construction of oxide heterointerfaces with designed polyhedral connections. a) Schematic illustration of oxygen pumping across brownmillerite/perovskite heterointerfaces due to mismatched chemical potential of oxygen ions. Two types of heterointerfaces, namely the O_h-O_h and the T_d-O_h heterointerfaces, can be formed based on the terminated polyhedron in the brownmillerite layer. The red arrows represent the directions of oxygen migration across two distinct heterointerfaces. b,c) Reflection-high-energy-electron diffraction (RHEED) intensity oscillations of the specular spot during the growth of b) brownmillerite $CaFeO_{2.5}$ (CFO) and c) perovskite $La_{0.7}Sr_{0.3}MnO_3$ (LSMO) layers, respectively. The substrate is TiO_2-terminated $SrTiO_3$ (STO) (001). The right panel shows the growth modes of CFO and LSMO, in which the CFO layer is grown by the combined O_h and T_d layers and terminated by the T_d layer. On the other hand, the LSMO layer is grown with O_h blocks. d,e) Schematic illustrations of d) the T_d-O_h and e) the O_h-O_h heterointerfaces, in which the growth sequence of LSMO and CFO layers is switched.

and "red shift" of the Mn L_3-edge can be observed for the T_d-O_h and the O_h-O_h heterointerfaces, respectively, as compared to that of the pristine LSMO film. Such energy shift of the Mn L_3-edge indicates a higher (lower) valence state in Mn ions at the T_d-O_h (the O_h-O_h) heterostructure. It is important to note that both charge transfer and oxygen ion migration can lead to a change in valence. However, the charge transfer driven by the "polar catastrophe"[40,41] mechanism, arising from the electrostatic potential gradient, will lead to a higher valence state in Mn ions near the O_h-O_h heterointerfaces than the T_d-O_h heterointerfaces (Figure S4, Supporting Information), which is opposite to what we observed. Thus, the scenario of charge reconstruction can be excluded. Furthermore, it is intriguing that the valence state of all five-unit-cell Mn ions is homogeneously modified, which further excludes the charge transfer mechanism due to the short-range screening effects. Additionally, the oxygen *K*-edge exhibits a significant right shift of pre-edge peak position in the O_h-O_h sample as comparing with the T_d-O_h sample, further confirming the formation of oxygen vacancies (Figure S5, Supporting Information). Therefore, the different electronic states in these two heterointerfaces should be attributed to the migrations of oxygen ions. In stark contrast with the LSMO sample in O_h-O_h

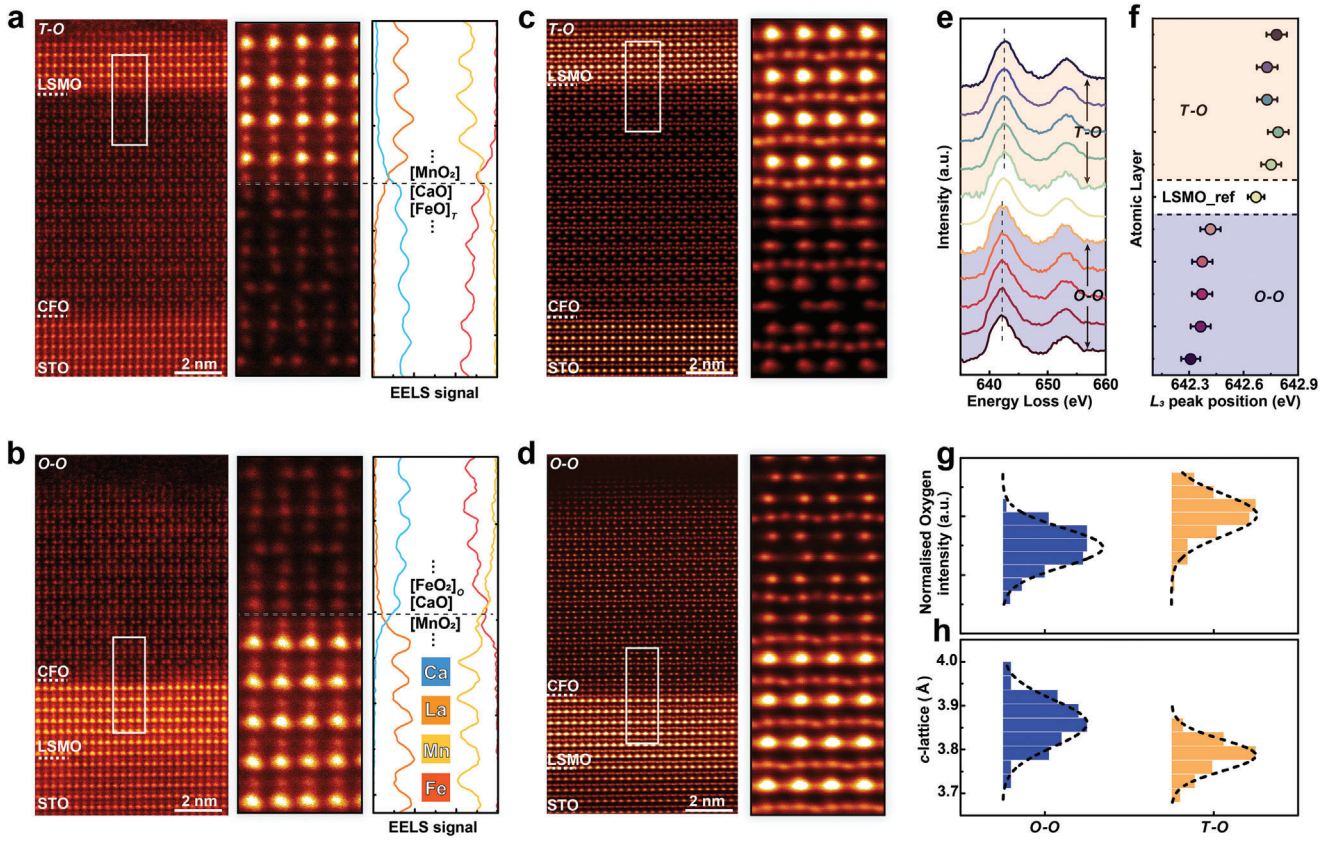

Figure 2. Structural insights of the controlled dual-directional oxygen-ion pumping. a,b) HAADF-STEM images of a) the T_d-O_h and b) the O_h-O_h heterointerfaces, respectively. The left panel is the cross-sectional view of the heterostructures. The middle panel shows a zoom-in view across the interface of LSMO and CFO (the white square region), where the polyhedral connection can be nicely resolved. The right panel is the atomic-layer-dependent EELS intensity of Ca $L_{3,2}$ (blue line), La $M_{5,4}$ (yellow line), Mn $L_{3,2}$ (yellow line) and Fe $L_{3,2}$ (red line) edges extracted along depth direction (see raw data in Figure S2, Supporting Information). The black dotted line represents the interface. c,d) ABF-STEM images of c) the T_d-O_h and d) the O_h-O_h heterointerfaces. e) Atomic-layer-dependent EELS signals measured at Mn $L_{3,2}$ edges for both the T_d-O_h and the O_h-O_h heterointerfaces, respectively. The dashed lines help distinguish the variation of the positions of L_3 peak for two different LSMO layers. f) Fitted L_3 peak positions of different atomic layers extracted from T_d-O_h and O_h-O_h heterointerfaces. Lorentz function was used to fit the peak position. The LSMO reference spectra comes from LSMO/STO heterostructure. g) Normalized intensity of oxygen column and h) *c*-lattice constant of LSMO layer for samples with O_h-O_h and T_d-O_h heterointerfaces. The oxygen intensity is normalized by the intensity of Mn site.

heterointerface with oxygen vacancy, we deduce that the LSMO in the T_d-O_h heterointerface has slightly excess oxygen content. We note that oxygen non-stoichiometry is widely observed in perovskite oxides such as titanates and manganites, showing wide range of functionalities.[42] Particularly, studies in manganites demonstrated that the non-stoichiometric $LaMnO_{3+\delta}$[43,44] and $La_{1-x}Sr_xMnO_{3+\delta}$[45,46] samples can remain in the perovskite structures, while their magnetic and electronic properties are dramatically modified predominately due to the charge doping effect. However, the direct imaging of the excess oxygen ion forms a much challenging work to pursue for us. The recent work from Chen et al.[47] demonstrated that single oxygen vacancy can be identify from the oxide samples, which should be able to shed new light for a future study on the current work. We further estimate the change of oxygen content based on the valence state of Mn measured by EELS. We note that the L_3/L_2 ratio of Mn *L*-edges forms a widely accepted caliber to evaluate the valence state of Mn ions in manganites.[48] As shown in Figure S6, Supporting Information, the valence state difference (δ) of Mn ions is estimated to be ≈0.3 between O_h-O_h and T_d-O_h heterointerfaces. With that, we estimate that the LSMO sample with T_d-O_h heterointerface has 0.15 more atomic oxygen/c.f. than the sample with O_h-O_h heterointerface. It is noted that majority of this difference should be attributed to the oxygen vacancy formation in O_h-O_h heterointerfaces, as indicated by the larger valence difference between reference LSMO sample and sample with O_h-O_h heterointerface (Figure 2f).

In addition to the change of EELS signal, we also observed variation of oxygen column intensity in the ABF-STEM image. We normalized the intensity of Mn atoms in the two heterointerfaces as a benchmark and found a lower oxygen contrast in LSMO layer near the O_h-O_h heterointerface (Figure 2g). This result is qualitatively consistent with the lower oxygen content in O_h-O_h heterointerface. Additionally, oxygen vacancy formation in LSMO is expected to elongate its *c*-lattice due to the combined chemical expansion and in-plane epitaxial strain, which is confirmed by the measured lattice parameters in the LSMO layers (Figure 2h). Moreover, we observed no measurable change of Fe $L_{3,2}$-edges in

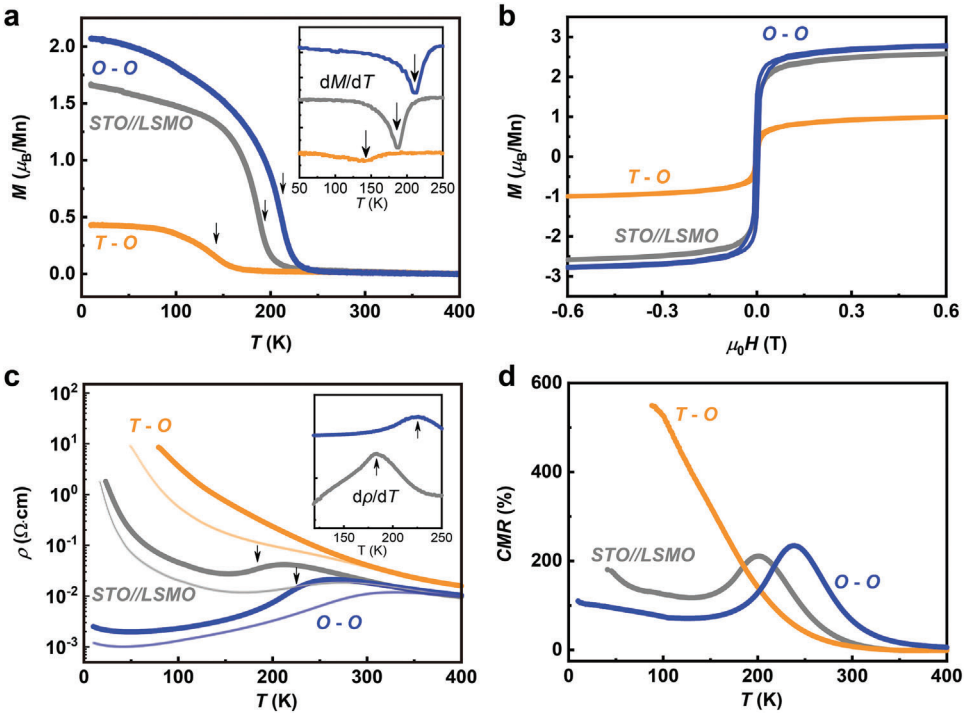

Figure 3. Evolution of magnetic and electronic states of LSMO heterostructures due to the formation of different polyhedral connections. a) Temperature-dependent magnetizations of LSMO heterostructures measured with field cooling at 0.01 T. The yellow and blue curves represent the results taken from the samples with the T_d-O_h and the O_h-O_h heterointerfaces, while the data on LSMO//STO layer (gray curve) are used for comparison. b) Magnetic hysteresis loops for LSMO samples measured at 100 K. The magnetic field is applied along the in-plane [100] direction of the substrate. c) Temperature dependent electrical resistivity of the LSMO layers. d) Temperature-dependent colossal magnetoresistance (CMR) data for different LSMO layers. The CMR is defined as $(R(0)-R(B))/R(B)$, where $R(0)$ and $R(B)$ are the resistances taken at zero and 9 T magnetic field applied along the out-of-plane direction. The thickness of LSMO layers is 7 u.c. for all samples shown in this figure.

two heterointerfaces (Figure S7, Supporting Information), indicating that the oxygen content remains unchanged in CFO layers. These results suggest distinct oxygen ionic migration directions of LSMO layers at the O_h-O_h and the T_d-O_h heterointerfaces, in which CFO layer can be considered as a "oxygen pump" to transfer oxygen ions into the LSMO layer, instead of taking the role as oxygen ion acceptor or donor, as we illustrated in Figure 1a.

Since the magnetic and electronic states of LSMO are strongly correlated with its oxygen content, we further studied/compared the magnetic and electronic properties of the O_h-O_h and the T_d-O_h heterostructures. The temperature-dependent magnetization measurements (**Figure 3a**) show that the Curie temperature (T_C) of LSMO with the O_h-O_h (the T_d-O_h) heterointerfaces ascends (descends) to ≈220 K (≈150 K), compared to the T_C of ≈200 K in pristine state (7 u.c. thick). The *M*-*H* measurements (Figure 3b) also prove the consistent enhancement (reduction) of the saturation magnetizations of LSMO with the O_h-O_h (the T_d-O_h) heterointerfaces compared to the pristine state. In agreement with the corresponding magnetic properties, distinct resistivity properties (Figure 3c,d) of LSMO were also observed with the T_d-O_h and the O_h-O_h heterointerfaces, exhibiting insulating and conducting behaviors, respectively. Furthermore, the O_h-O_h sample shows an enhanced metallicity and a higher metal-insulator transition temperature (T_{MIT}), consistent with its enhanced magnetization. We note that the magnetic order and insulator-metal transition in the mixed-valent manganites strongly depend on the doping level and the lattice distortion. Considering the posibility that extra hole doping caused by Sr surface segregation[49–53] and the strain[54–56] on our thin LSMO layer, it is reasonable to expect that our pristine LSMO (Sr = 0.3) locates equivalently at the over-doping regime instead of the optimally doped regime. In this scenario, the oxygen deficient will bring the sample back to the optimal doping regime through electron doping. Additionally, the oxygen migration also plays a key role on the lattice structure. We observed that the oxygen deficient LSMO film has a larger *c*-lattice constant (Figure 2h), which can reduce the octahedral tilt and then subsequently enhance the *p*-*d* hybridization and widen the bandwidth, and the correlation between such structure change and enhanced magnetization has been revealed in previously studies.[57,58] We note that the charge doping and structural change both favor the enhanced magnetization, as observed in LSMO samples with the O_h-O_h interface. Figure S9, Supporting Information further displays the thickness-dependent T_C and T_{MIT} for both interfaces with various LSMO thicknesses, where the difference between the O_h-O_h and the T_d-O_h heterointerfaces is more pronounced for thinner samples and damps gradually as the thickness of LSMO increases to about 20 u.c. (≈8 nm). This trend indicates that the oxygen ions migration induced by the brownmillerite oxygen "pump" plays a significant role with extended length scale compared to the conventional interfacial effects (e.g., the interfacial oxygen octahedral coupling[59–61] and electronic reconstruction[62,63])

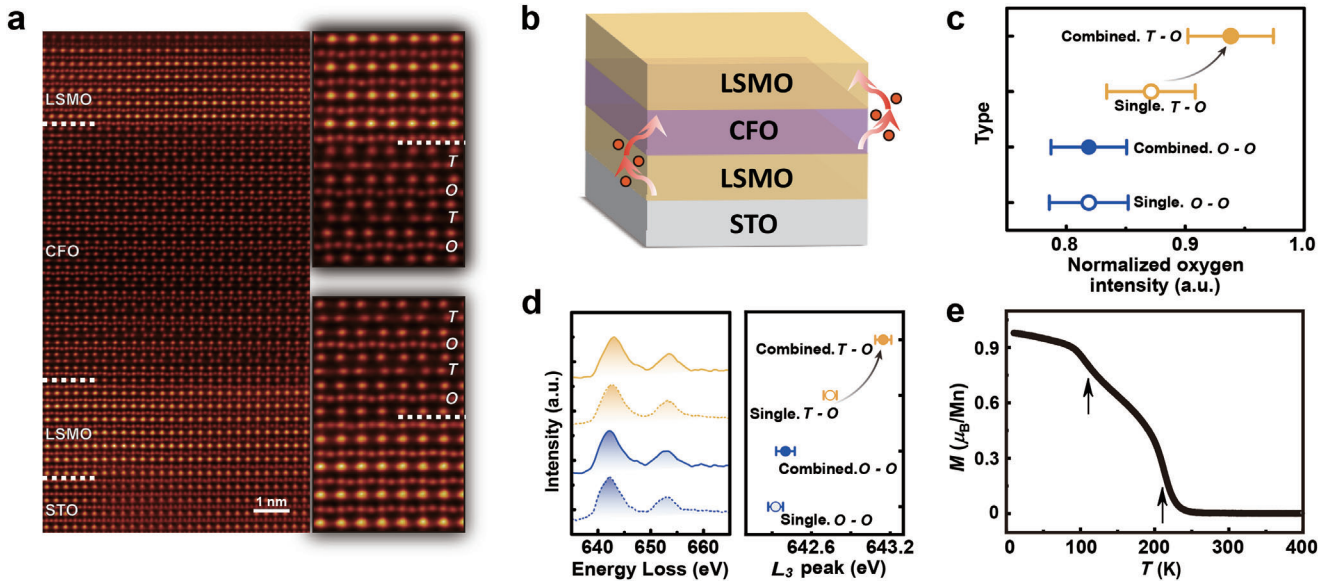

Figure 4. Oxygen-ion pumping with the combination of the T_d-O_h and the O_h-O_h heterointerfaces. a) ABF-STEM image (left) of STO//LSMO/CFO/LSMO system, where both the T_d-O_h (upper right panel) and the O_h-O_h (lower right panel) heterointerfaces are nicely constructed. b) Schematic illustration of oxygen-ion pumping across the T_d-O_h and the O_h-O_h heterointerfaces. The red arrows indicate the direction of oxygen migration across the heterostructure. c) Comparison of normalized oxygen column intensity in LSMO layers with single (the T_d-O_h and the O_h-O_h, hollow circles) and combined (solid circles) heterointerfaces. The yellow and blue colors represent the T_d-O_h and the O_h-O_h interfaces, respectively. d) Evolution of valence states in Mn ions across the interfaces. The left panel shows the comparison of EELS spectra in Mn $L_{3,2}$ edges between single (dotted lines) and combined (solid lines) heterointerfaces. The right panel is fitted L_3 peak positions of single (hollow circles) and combined (solid circles) heterointerfaces. e) Temperature-dependent magnetization of LSMO/CFO/LSMO tri-layer heterostructure. The magnetization was calculated by averaging among both the top and the bottom LSMO layers. The data reveal two distinct transitions as highlighted by the arrows.

that are confined within just a few unit cells from the interface.

We note that the chemical potential difference for electron and oxygen ion across the interface leads to respectively electron and oxygen ion diffusion across the interface, which however behaves very different. In the case for only electron diffusion such as at P-N junction, the different Fermi energies (i.e., chemical potential for electron) between materials lead to charge diffusion, generating an interfacial electric field and thus an electrostatic potential difference across the interface, which counter-balance the initial Fermi level difference to form an equilibrium state with localized space charge. In this case, the transferred electron exponentially decays from the interface. Similarly, for an idea case with only oxygen ion diffusion such as at the interface between electrode and electrolyte, a space charge layer (the so-called double layer) can be formed, in which the developed potential difference can also "screen" the initial chemical potential difference. While in a more practical situation, both oxygen ion and electron diffusion can simuatniously occur between two materials, such as in the case with short-circuited anode and cathode, in which the screen effect is less effective since both materials tend to remain charge neutral with the accompanied electron transfer. Consequently, although the chemical potential difference can be very close between the electron and oxygen ion, the oxygen ion can diffuse over much greater distance, leading to extended influenced length scale.

With the brownmillerite CFO acting as the "oxygen pump," we designed the sandwiched STO//LSMO/CFO/LSMO heterostructure to further enhance the "pumping" effect by combining both heterointerfaces in the same system. As shown in **Figure** 4a and S10, Supporting Information, the O_h-O_h and the T_d-O_h heterointerfaces of the sandwiched heterostructures were confirmed by the ABF-STEM images and the EELS measurements, verifying the robust nature of this growth strategy. Due to the collective contributions of the O_h-O_h and the T_d-O_h heterointerface to the oxygen migration, their combination is expected to enhance the oxygen potential gradient within CFO, leading to a more significant pumping effect. Furthermore, the oxygen content would become distinctively different for the top and the bottom LSMO layers (Figure 4b). This scenario is verified by the measurements of the oxygen contrast and Mn valence states with the ABF-STEM images and the EELS analysis, respectively. Interestingly, this enhancement of "pumping effect" is not symmetrically distributed between the top (with the T_d-O_h interface) and the bottom LSMO layers (with the O_h-O_h interface). The top LSMO layer takes the predominant share, which can be observed from the oxygen contrast, Mn valence states and magnetic properties. The difference of the oxygen contrast (Figure 4c) of the O_h-O_h and the T_d-O_h in the combined heterointerface system, is more substantial than that of the single heterointerface. Specifically, the top LSMO layer (with the T_d-O_h interface) shows a more prominent "blue shift" of the Mn L_3-edge from that of the bottom LSMO layer (with the O_h-O_h interface) (Figure 4d) as compared with the effect of their corresponding single heterointerfaces, which implies a cooperatively enhanced valence change in this tri-layer structure. Such an enhanced difference in oxygen stoichiometry between the top and the bottom LSMO layers leads to further magnetic change between these two layers. As shown in Figure 4e, two distinct

magnetic transitions can be clearly identified in the temperature-dependent magnetization measurements, which are individually contributed by the top and the bottom LSMO layers. Specifically, the T_C of the T_d-O_h LSMO layer in the combined heterointerface is further reduced as compared to the corresponding single heterostructure, and the T_C of the O_h-O_h LSMO layer remains almost unchanged, which is consistent with the change of oxygen concentration in these two layers. The results of this sandwiched structure clearly demonstrate that the brownmillerite CFO can serve as an efficient "oxygen pump" to modulate the oxygen migration between its neighbored layers, and this structure can be conveniently extended and integrated to other complex oxide heterostructures to manipulate or even create new magnetic and electronic states through oxygen ionic evolution.

3. Conclusion

To summarize, we propose and demonstrate the possibility on control of oxygen ionic migration across the perovskite LSMO and brownmillerite CFO heterointerfaces, where the brownmillerite CFO layer acts as an "oxygen pump" to its neighbored perovskite LSMO layer. Consequently, the magnetic and electronic properties of LSMO layers was successfully manipulated depending on the polyhedral stacking sequence across the interface, which determines the oxygen ionic migration direction across the interface. This work not only highlights the critical role of oxygen ionic evolution on the electronic and magnetic states within complex oxides, but also opens a new avenue to control the oxygen ionic migration across oxide heterointerfaces for tailored electronic states and functionalities.

4. Experimental Section

Sample Fabrication: Complex oxide heterostructures were grown by a home-built pulsed laser deposition (PLD) system (KrF, $\lambda = 248$ nm) while utilizing high-pressure reflective high-energy electron diffraction (RHEED) spectroscopy to monitor the growth. Single crystal $SrTiO_3$ (STO) (001) substrates were used for the growth, which were treated with buffered HF acid etching and thermal annealing (at 950 °C) to obtain TiO_2 (*B* site)-terminated surfaces (Figure S1, Supporting Information). $CaFeO_{2.5}$ (CFO) thin films were deposited at a growth temperature of 575 °C and an oxygen pressure of 0.12 mbar, and the laser energy density was fixed at 1.3 J cm^{-2} at the ceramic target surface with the repetition rate at 3 Hz. $La_{0.7}Sr_{0.3}MnO_3$ (LSMO) thin films were deposited at a growth temperature of 660 °C and an oxygen pressure of 0.18 mbar, and the laser energy density was fixed at 1.2 J cm^{-2} with the repetition rate at 1 Hz. After the deposition, the samples were cooled down to room temperature at a cooling rate of 10 °C per minute and an oxygen pressure of 0.18 mbar.

Scanning Transmission Electron Microscopy: STEM samples were prepared using a focused ion beam (FIB) instrument (Zeiss Crossbeam). The samples were thinned down to 50 nm using an accelerating voltage of 30 kV with a decreasing current from 240 to 50 pA, followed by a fine polish treatment with an accelerating voltage of 5 kV with a current of 20 pA. Subsequently, the FIB lamella was cleaned by Nanomill with low-voltage 900 V at 120 μA and then 500 V and 100 μA to remove the amorphous layer. We note that through this low-voltage cleaning, the amorphous layer can be well reduced as evidenced by the high quality STEM images. The HAADF-STEM and ABF-STEM images were acquired on an FEI Titan Cubed Themis 60–300 (operated at 300 kV), capable of recording high-resolution STEM images with the spatial resolution of ≈0.059 nm. The microscope was equipped with a high brightness electron gun (X-FEG with monochromator), a spherical aberration corrector, and a post-column imaging energy filter (Gatan Quantum 965 Spectrometer). The collection angle of the HAADF and ABF detector was ≈48–200 mrad and 6–48 mrad, respectively. Quantitative measurements of c-lattice, bond angle and oxygen intensity are based on fitting atomic position with AutoMap and custom-build code in python.[64] The Dual-EELS mode was employed to collect core-loss signals of multiple ions. The entrance aperture was 5 mm, the step size was 0.5 eV for elemental mapping, and 0.25 eV for measuring chemical shift. Data processing, including calibration of the zero-loss position, pre-edge background subtraction, removal of multiple scattering, and normalization, was carried out to extract EELS signals. All EELS data were processed using the Gatan Microscopy Suite 3.0 software package.

Macroscopic Magnetism and Electrical Transport Measurements: Temperature-dependent magnetization (*M*-*T*) measurements and magnetic hysteresis loop measurements were performed using a SQUID magnetometer (MPMS; Quantum Design), in which the maximum magnetic field is 7 T. A physical property measurement system (PPMS; Quantum Design) was used to measure the resistivity of the samples, in which the maximum magnetic field is 9 T. Four-probe method was used to eliminate the contact resistivity.

Supporting Information

Supporting Information is available from the Wiley Online Library or from the author.

Acknowledgements

Y.W. and Y.Z. contributed equally to this work. This study was financially supported by the National Key R&D Program of China (2023YFA1406400, 2021YFE0107900 and 2021YFA1400300), the National Natural Science Foundation of China (Nos. 52025024, 52388201 and 92163113), and the Beijing Nature Science Foundation (grant No. Z200007). J.Z. acknowledges support from Postdoctoral Fellowship Program of CPSF (GZB20240380).

Conflict of Interest

The authors declare no conflict of interest.

Data Availability Statement

The data that support the findings of this study are available in the supplementary material of this article.

Keywords

brownmillerite, complex oxide, heterointerface, manganite, oxygen ion

Received: April 25, 2024
Revised: July 27, 2024
Published online: August 20, 2024

[1] H. Y. Hwang, Y. Iwasa, M. Kawasaki, B. Keimer, N. Nagaosa, Y. Tokura, *Nat. Mater.* **2012**, *11*, 103.
[2] A. Ohtomo, H. Y. Hwang, *Nature* **2004**, *427*, 423.
[3] A. Tsukazaki, A. Ohtomo, T. Kita, Y. Ohno, H. Ohno, M. Kawasaki, *Science* **2007**, *315*, 1388.

[4] K. Ueda, H. Tabata, T. Kawai, *Science* **1998**, *280*, 1064.
[5] Y. Wang, Q. He, W. Ming, M.-H. Du, N. Lu, C. Cafolla, J. Fujioka, Q. Zhang, D. Zhang, S. Shen, Y. Lyu, A. T. N'Diaye, E. Arenholz, L. Gu, C. Nan, Y. Tokura, S. Okamoto, P. Yu, *Phys. Rev. X* **2020**, *10*, 021030.
[6] J. H. Haeni, P. Irvin, W. Chang, R. Uecker, P. Reiche, Y. L. Li, S. Choudhury, W. Tian, M. E. Hawley, B. Craigo, A. K. Tagantsev, X. Q. Pan, S. K. Streiffer, L. Q. Chen, S. W. Kirchoefer, J. Levy, D. G. Schlom, *Nature* **2004**, *430*, 758.
[7] J. P. Locquet, J. Perret, J. Fompeyrine, E. Mächler, J. W. Seo, G. Van Tendeloo, *Nature* **1998**, *394*, 453.
[8] J. Chakhalian, J. W. Freeland, G. Srajer, J. Strempfer, G. Khaliullin, J. C. Cezar, T. Charlton, R. Dalgliesh, C. Bernhard, G. Cristiani, H. U. Habermeier, B. Keimer, *Nat. Phys.* **2006**, *2*, 244.
[9] P. Yu, J. S. Lee, S. Okamoto, M. D. Rossell, M. Huijben, C. H. Yang, Q. He, J. X. Zhang, S. Y. Yang, M. J. Lee, Q. M. Ramasse, R. Erni, Y. H. Chu, D. A. Arena, C. C. Kao, L. W. Martin, R. Ramesh, *Phys. Rev. Lett.* **2010**, *105*, 027201.
[10] N. Nakagawa, H. Y. Hwang, D. A. Muller, *Nat. Mater.* **2006**, *5*, 204.
[11] Y. Hotta, T. Susaki, H. Y. Hwang, *Phys. Rev. Lett.* **2007**, *99*, 236805.
[12] M. Takizawa, Y. Hotta, T. Susaki, Y. Ishida, H. Wadati, Y. Takata, K. Horiba, M. Matsunami, S. Shin, M. Yabashi, K. Tamasaku, Y. Nishino, T. Ishikawa, A. Fujimori, H. Y. Hwang, *Phys. Rev. Lett.* **2009**, *102*, 236401.
[13] D. Yi, P. Yu, Y.-C. Chen, H.-H. Lee, Q. He, Y.-H. Chu, R. Ramesh, *Adv. Mater.* **2019**, *31*, 1806335.
[14] A. Kalabukhov, R. Gunnarsson, J. Börjesson, E. Olsson, T. Claeson, D. Winkler, *Phys. Rev. B* **2007**, *75*, 121404.
[15] W. Siemons, G. Koster, H. Yamamoto, W. A. Harrison, G. Lucovsky, T. H. Geballe, D. H. A. Blank, M. R. Beasley, *Phys. Rev. Lett.* **2007**, *98*, 196802.
[16] Y. Chen, N. Pryds, J. E. Kleibeuker, G. Koster, J. Sun, E. Stamate, B. Shen, G. Rijnders, S. Linderoth, *Nano Lett.* **2011**, *11*, 3774.
[17] H. Guo, J.-o. Wang, X. He, Z. Yang, Q. Zhang, K.-j. Jin, C. Ge, R. Zhao, L. Gu, Y. Feng, W. Zhou, X. Li, Q. Wan, M. He, C. Hong, Z. Guo, C. Wang, H. Lu, K. Ibrahim, S. Meng, H. Yang, G. Yang, *Adv. Mater. Interfaces* **2016**, *3*, 1500753.
[18] S. Kumari, N. Mottaghi, C.-Y. Huang, R. Trappen, G. Bhandari, S. Yousefi, G. Cabrera, M. S. Seehra, M. B. Holcomb, *Sci. Rep.* **2020**, *10*, 3659.
[19] J. M. Tarascon, B. G. Bagley, *MRS Bull.* **1989**, *14*, 53.
[20] J. Jeong, N. Aetukuri, T. Graf, T. D. Schladt, M. G. Samant, S. S. P. Parkin, *Science* **2013**, *339*, 1402.
[21] N. Lu, Z. Zhang, Y. Wang, H.-B. Li, S. Qiao, B. Zhao, Q. He, S. Lu, C. Li, Y. Wu, M. Zhu, X. Lyu, X. Chen, Z. Li, M. Wang, J. Zhang, S. C. Tsang, J. Guo, S. Yang, J. Zhang, K. Deng, D. Zhang, J. Ma, J. Ren, Y. Wu, J. Zhu, S. Zhou, Y. Tokura, C.-W. Nan, J. Wu, et al., *Nat. Energy* **2022**, *7*, 1208.
[22] K. P. Kelley, A. N. Morozovska, E. A. Eliseev, Y. Liu, S. S. Fields, S. T. Jaszewski, T. Mimura, S. Calderon, E. C. Dickey, J. F. Ihlefeld, S. V. Kalinin, *Nat. Mater.* **2023**, *22*, 1144.
[23] O. N. Tufte, P. W. Chapman, *Phys. Rev.* **1967**, *155*, 796.
[24] R. J. Cava, B. Batlogg, C. H. Chen, E. A. Rietman, S. M. Zahurak, D. Werder, *Nature* **1987**, *329*, 423.
[25] J. Zhang, S. Shen, D. Puggioni, M. Wang, H. Sha, X. Xu, Y. Lyu, H. Peng, W. Xing, L. N. Walters, L. Liu, Y. Wang, D. Hou, C. Xi, L. Pi, H. Ishizuka, Y. Kotani, M. Kimata, H. Nojiri, T. Nakamura, T. Liang, D. Yi, T. Nan, J. Zang, Z. Sheng, Q. He, S. Zhou, N. Nagaosa, C.-W. Nan, Y. Tokura, et al., *Nat. Mater.* **2024**, *23*, 912.
[26] H. Jeen, W. S. Choi, M. D. Biegalski, C. M. Folkman, I. C. Tung, D. D. Fong, J. W. Freeland, D. Shin, H. Ohta, M. F. Chisholm, H. N. Lee, *Nat. Mater.* **2013**, *12*, 1057.
[27] N. Lu, P. Zhang, Q. Zhang, R. Qiao, Q. He, H.-B. Li, Y. Wang, J. Guo, D. Zhang, Z. Duan, Z. Li, M. Wang, S. Yang, M. Yan, E. Arenholz, S. Zhou, W. Yang, L. Gu, C.-W. Nan, J. Wu, Y. Tokura, P. Yu, *Nature* **2017**, *546*, 124.
[28] Q. Wang, Y. D. Gu, W. X. Zhu, L. Han, F. Pan, C. Song, *Adv. Funct. Mater.* **2021**, *31*, 2100738.
[29] Y. Tsujimoto, C. Tassel, N. Hayashi, T. Watanabe, H. Kageyama, K. Yoshimura, M. Takano, M. Ceretti, C. Ritter, W. Paulus, *Nature* **2007**, *450*, 1062.
[30] S. Inoue, M. Kawai, N. Ichikawa, H. Kageyama, W. Paulus, Y. Shimakawa, *Nat. Chem.* **2010**, *2*, 213.
[31] D. Li, K. Lee, B. Y. Wang, M. Osada, S. Crossley, H. R. Lee, Y. Cui, Y. Hikita, H. Y. Hwang, *Nature* **2019**, *572*, 624.
[32] A. A. Emery, C. Wolverton, *Sci. Data* **2017**, *4*, 170153.
[33] Y. Li, W. C. Chueh, *Annu. Rev. Mater. Res.* **2018**, *48*, 137.
[34] E.-J. Guo, Y. Liu, C. Sohn, R. D. Desautels, A. Herklotz, Z. Liao, J. Nichols, J. W. Freeland, M. R. Fitzsimmons, H. N. Lee, *Adv. Mater.* **2018**, *30*, 1705904.
[35] Y. Park, H. Sim, M. Jo, G.-Y. Kim, D. Yoon, H. Han, Y. Kim, K. Song, D. Lee, S.-Y. Choi, J. Son, *Nat. Commun.* **2020**, *11*, 1401.
[36] Y. Park, H. Sim, K.-Y. Doh, M. Jo, D. Lee, S.-Y. Choi, J. Son, *Nano Lett.* **2022**, *22*, 9306.
[37] B. Cui, C. Song, F. Li, X. Y. Zhong, Z. C. Wang, P. Werner, Y. D. Gu, H. Q. Wu, M. S. Saleem, S. S. P. Parkin, F. Pan, *Phys. Rev. Appl.* **2017**, *8*, 044007.
[38] A. Gloter, J. Ingrin, D. Bouchet, C. Colliex, *Phys. Rev. B* **2000**, *61*, 2587.
[39] T. Das, J. D. Nicholas, Y. Qi, *J. Mater. Chem. A* **2017**, *5*, 4493.
[40] H. Boschker, J. Verbeeck, R. Egoavil, S. Bals, G. van Tendeloo, M. Huijben, E. P. Houwman, G. Koster, D. H. A. Blank, G. Rijnders, *Adv. Funct. Mater.* **2012**, *22*, 2235.
[41] E. J. Guo, M. A. Roldan, T. Charlton, Z. Liao, Q. Zheng, H. Ambaye, A. Herklotz, Z. Gai, T. Z. Ward, H. N. Lee, M. R. Fitzsimmons, *Adv. Funct. Mater.* **2018**, *28*, 1800922.
[42] M. A. Peña, J. L. G. Fierro, *Chem. Rev.* **2001**, *101*, 1981.
[43] B. C. Tofield, W. R. Scott, *J. Solid State Chem.* **1974**, *10*, 183.
[44] N. Kamegashira, Y. Miyazaki, H. Yamamoto, *Mater. Chem. Phys.* **1984**, *11*, 187.
[45] J. Mizusaki, N. Mori, H. Takai, Y. Yonemura, H. Minamiue, H. Tagawa, M. Dokiya, H. Inaba, K. Naraya, T. Sasamoto, T. Hashimoto, *Solid State Ionics* **2000**, *129*, 163.
[46] L. Rørmark, K. Wiik, S. Stølen, T. Grande, *J. Mater. Chem.* **2002**, *12*, 1058.
[47] Z. Dong, M. Huo, J. Li, J. Li, P. Li, H. Sun, L. Gu, Y. Lu, M. Wang, Y. Wang, Z. Chen, *Nature* **2024**, *630*, 847.
[48] M. Varela, M. P. Oxley, W. Luo, J. Tao, M. Watanabe, A. R. Lupini, S. T. Pantelides, S. J. Pennycook, *Phys. Rev. B* **2009**, *79*, 085117.
[49] H. Dulli, P. A. Dowben, S. H. Liou, E. W. Plummer, *Phys. Rev. B* **2000**, *62*, R14629.
[50] R. Bertacco, J. P. Contour, A. Barthélemy, J. Olivier, *Surf. Sci.* **2002**, *511*, 366.
[51] H. Kumigashira, K. Horiba, H. Ohguchi, K. Ono, M. Oshima, N. Nakagawa, M. Lippmaa, M. Kawasaki, H. Koinuma, *Appl. Phys. Lett.* **2003**, *82*, 3430.
[52] T. T. Fister, D. D. Fong, J. A. Eastman, P. M. Baldo, M. J. Highland, P. H. Fuoss, K. R. Balasubramaniam, J. C. Meador, P. A. Salvador, *Appl. Phys. Lett.* **2008**, *93*, 151904.
[53] R. Herger, P. R. Willmott, C. M. Schlepütz, M. Björck, S. A. Pauli, D. Martoccia, B. D. Patterson, D. Kumah, R. Clarke, Y. Yacoby, M. Döbeli, *Phys. Rev. B* **2008**, *77*, 085401.
[54] Y. Konishi, Z. Fang, M. Izumi, T. Manako, M. Kasai, H. Kuwahara, M. Kawasaki, K. Terakura, Y. Tokura, *J. Phys. Soc. Jpn.* **1999**, *68*, 3790.
[55] Z. Fang, I. V. Solovyev, K. Terakura, *Phys. Rev. Lett.* **2000**, *84*, 3169.
[56] Z. Fang, K. Terakura, *J. Phys. Soc. Jpn.* **2001**, *70*, 3356.

[57] Z. Liao, N. Gauquelin, R. J. Green, S. Macke, J. Gonnissen, S. Thomas, Z. Zhong, L. Li, L. Si, S. Van Aert, P. Hansmann, K. Held, J. Xia, J. Verbeeck, G. Van Tendeloo, G. A. Sawatzky, G. Koster, M. Huijben, G. Rijnders, *Adv. Funct. Mater.* **2017**, *27*, 1606717.
[58] S. Koohfar, A. S. Disa, M. S. J. Marshall, F. J. Walker, C. H. Ahn, D. P. Kumah, *Phys. Rev. B* **2017**, *96*, 024108.
[59] A. Y. Borisevich, H. J. Chang, M. Huijben, M. P. Oxley, S. Okamoto, M. K. Niranjan, J. D. Burton, E. Y. Tsymbal, Y. H. Chu, P. Yu, R. Ramesh, S. V. Kalinin, S. J. Pennycook, *Phys. Rev. Lett.* **2010**, *105*, 087204.
[60] J. M. Rondinelli, S. J. May, J. W. Freeland, *MRS Bull.* **2012**, *37*, 261.
[61] Z. Liao, M. Huijben, Z. Zhong, N. Gauquelin, S. Macke, R. J. Green, S. Van Aert, J. Verbeeck, G. Van Tendeloo, K. Held, G. A. Sawatzky, G. Koster, G. Rijnders, *Nat. Mater.* **2016**, *15*, 425.
[62] J. W. Freeland, J. Chakhalian, A. V. Boris, J. M. Tonnerre, J. J. Kavich, P. Yordanov, S. Grenier, P. Zschack, E. Karapetrova, P. Popovich, H. N. Lee, B. Keimer, *Phys. Rev. B* **2010**, *81*, 094414.
[63] A. Bhattacharya, S. J. May, S. G. E. te Velthuis, M. Warusawithana, X. Zhai, B. Jiang, J. M. Zuo, M. R. Fitzsimmons, S. D. Bader, J. N. Eckstein, *Phys. Rev. Lett.* **2008**, *100*, 257203.
[64] M. Nord, P. E. Vullum, I. MacLaren, T. Tybell, R. Holmestad, *Adv. Struct. Chem. Imaging* **2017**, *3*, 9.